Journal of Materials Chemistry C

ROYAL SOCIETY OF CHEMISTRY

PAPER

View Article Online
View Journal | View Issue

Cite this: J. Mater. Chem. C, 2025, 13, 16427

A benzothiadiazole-decorated UiO-68 metal–organic framework for diclofenac and ibuprofen luminescence sensing and adsorption in wastewater†

Giacomo Provinciali, [a] Giulio Bicchierai, [a] Agostina Lina Capodilupo, [b] Anna Mauri, [c] Jia Fu, [d] Dahuan Liu, *[d] Giuliano Giambastiani, [aef] Giulia Tuci, [af] Simona Galli, *[cf] Clara Piccirillo *[b] and Andrea Rossin *[af]

The Zr^{IV} mixed-linker metal–organic framework (MIXMOF) $[Zr_6O_4(OH)_7(H_2O)_3(TPDC)_3(BTDZ)_{1.5}]$ [**Zr_BTDZ**; H_2TPDC = (*p*-terphenyl)-4,4″-dicarboxylic acid, H_2BTDZ = 4,4′-(benzothiadiazole-4,7-diyl)dibenzoic acid], exhibiting an UiO-68-type crystal structure, was prepared through direct synthesis under solvothermal conditions. **Zr_BTDZ** is fully microporous, with pore sizes in the range of $18 \leq w \leq 22$ Å and a BET SSA of 3770 $m^2\ g^{-1}$. The benzothiadiazole ring imparts luminescence to the material, showing a very intense ligand-centered emission band at λ_{max} = 516 nm (upon UV excitation at λ = 328 nm) falling in the light green visible region. **Zr_BTDZ** was exploited as a luminescent sensor and an adsorbent of the pharmaceuticals diclofenac sodium (DCF) and ibuprofen sodium (IBR) in aqueous solutions. No λ_{max} variation occurs upon interaction with the drugs; while for DCF an emission intensity decrease is observed with increasing pollutant concentration in solution, the opposite holds for IBR. The limit of detection is 4.1×10^{-6} and 1.6×10^{-6} M for DCF and IBR, respectively, while the maximum adsorption capacity at ambient temperature (X_m) is 100 and 161 mg g^{-1} for DCF and IBR, respectively. The non-covalent host–guest interactions were disclosed through DFT optimizations of the [DCF@**Zr_BTDZ**] and [IBR@**Zr_BTDZ**] adducts; hydrogen bonding between the μ-OH groups of the $[Zr_6]$ inorganic building unit and the DCF/IBR carboxylate groups occurs, together with π–π T-shaped/π–cation interactions between the aromatic rings/Na^+ ion of IBR/DCF and the MOF organic linkers. The calculated adduct formation energies (ΔE_{DCF} = −192.5 kJ mol^{-1}; ΔE_{IBR} = −228.2 kJ mol^{-1}) are in line with the experimentally derived binding constants [$K_{b(DCF)}$ = 12.6×10^4 M^{-1}; $K_{b(IBR)}$ = 14.9×10^4 M^{-1}], showing a stronger interaction with IBR.

Received 7th April 2025,
Accepted 1st July 2025

DOI: 10.1039/d5tc01447f

rsc.li/materials-c

1. Introduction

Clean water is the driving force of life. It is an essential resource for human beings and nature and for regulating the climate. It is also crucial for the economy, agriculture and energy production. The availability of clean water is threatened by several factors, including pollution from industrial chemicals, pesticides, nutrients and pharmaceuticals. In the context of the European Green Deal,[1] the water framework directive provides the main framework and the objectives for water policy in Europe.[2] Urban wastewater is one of the main sources of water pollution if it is not collected and treated according to EU rules. It contains organic matter as well as nitrogen- and phosphorous-based inorganic compounds. These are removed when wastewater undergoes appropriate cleaning treatments, otherwise they can lead to eutrophication. Wastewater can also be contaminated with harmful chemicals which, when untreated and discharged into the environment, affect our health and damage our rivers,

[a] Istituto di Chimica dei Composti Organometallici (CNR-ICCOM), Via Madonna del Piano 10, Sesto Fiorentino (Firenze), 50019, Italy. E-mail: a.rossin@iccom.cnr.it
[b] CNR NANOTEC, Istituto di Nanotecnologia, Campus Ecotekne, Via Monteroni, 73100, Lecce, Italy. E-mail: clara.piccirillo@nanotec.cnr.it
[c] Dipartimento di Scienza e Alta Tecnologia, Università degli Studi dell'Insubria, Via Valleggio 11, 22100, Como, Italy. E-mail: simona.galli@uninsubria.it
[d] State Key Laboratory of Organic–Inorganic Composites, Beijing University of Chemical Technology, Beijing, 100029, China. E-mail: liudh@mail.buct.edu.cn
[e] Dipartimento di Chimica Ugo Schiff, Università di Firenze, Via della Lastruccia 3-13, 50019, Sesto Fiorentino (Firenze), Italy
[f] Consorzio Interuniversitario Nazionale per la Scienza e Tecnologia dei Materiali (INSTM), Via G. Giusti, 9, 50121, Firenze, Italy

† Electronic supplementary information (ESI) available: Additional characterization data of **Zr_BTDZ**: IR and XRF spectra, SEM-EDX analysis, Rietveld fitting plot, ^{1}H NMR spectrum of the digested solid (D_2SO_4/D_2O/DMSO-d_6), TG-DTG-DSC profile, absorption spectra of H_2BTDZ and **Zr_BTDZ**. Fitting plots of the UV-Vis data for the determination of the IBR/DCF K_b and LOD values, **Zr_BTDZ** HOCO-LUCO plots, DCF and IBR HOMO–LUMO plots. CCDC 2423400. For ESI and crystallographic data in CIF or other electronic format see DOI: https://doi.org/10.1039/d5tc01447f

lakes and coastal water;[3] 92% of toxic pollutants in wastewater come from the pharmaceutical and cosmetics sectors, and are not completely removed by the present wastewater treatment methods due to their chemical stability and different characteristics. Monitoring the presence of such molecules, as well as determining their concentrations, is crucial to assess water cleanness; it is therefore important to develop innovative methods for rapid and sensitive detection of specific pollutants, possibly combined with their efficient removal from wastewaters. Among the possible candidates, metal–organic frameworks (MOFs) represent an excellent class of compounds for this target.[4–8] MOFs represent ideal sensors and adsorbers for water contaminants, because of their high crystallinity, tuneable surface area and porosity combined with the extremely versatile combination of assorted organic linkers and metal nodes that can be selected for their synthesis. Zirconium carboxylate MOFs in particular, with their robust Zr–O coordination bonds, are water-tolerant and they can be easily exploited for applications in aqueous environments. In recent years, we have prepared a number of Zr^{IV} MOFs containing luminescent heterocyclic linkers for the detection and adsorption of the anti-inflammatory drug diclofenac sodium (DCF, in Italy commercialized as Voltaren®, Scheme S1, ESI†) in wastewater.[9,10] In the present work, we expand this family through the preparation of the mixed-linker MOF (MIXMOF) $[Zr_6O_4(OH)_7(H_2O)_3(TPDC)_3(BTDZ)_{1.5}]$ [**Zr_BTDZ**; H_2TPDC = (*p*-terphenyl)-4,4″-dicarboxylic acid, H_2BTDZ = 4,4′-(benzothiadiazole-4,7-diyl)-dibenzoic acid, Scheme 1], which contains the luminescent benzothiadiazole ring acting as antenna for the absorption of UV radiation and consequent fluorescence emission in the light green visible region. As demonstrated in the following, **Zr_BTDZ** exhibits good performance as a luminescent sensor and "sponge" not only toward DCF but also toward another anti-inflammatory drug that is often present in high concentrations in urban wastewater: ibuprofen sodium (IBR), commercially sold in Italy as Brufen® or Moment® (Scheme S1, ESI†).

2. Experimental

2.1. Materials and methods

Zirconium chloride ($ZrCl_4$, Sigma Aldrich), trifluoroacetic acid (CF_3COOH, HTFA, Sigma Aldrich), *N*,*N*-dimethylformamide (DMF, Sigma Aldrich), H_2TPDC (ChemSoon Ltd) and H_2BTDZ (ChemSoon Ltd) were purchased from commercial vendors and used as received. ^{1}H NMR spectra were recorded on a BRUKER AVANCE 400 MHz spectrometer, with chemical shifts (δ) reported in parts per million (ppm) downfield of tetramethylsilane (TMS) and calibrated against the residual protiated solvent resonance. FT-IR spectra (KBr pellets) were recorded on a PerkinElmer Spectrum BX Series FTIR spectrometer, in the 4000–400 cm^{-1} range, with a 2 cm^{-1} resolution. Thermogravimetric analyses (TG-DTG) were performed under a N_2 flow (100 mL min^{-1}) at a heating rate of 5 K min^{-1} with an EXSTAR Thermo Gravimetric Analyzer Seiko 6200. The latter was coupled with a ThermoStarTM GSD 301T mass spectrometer for mass analysis of the volatile species. Differential scanning calorimetry (DSC) was performed under a N_2 flow over the temperature range 293–1173 K with a heating rate of 5 K min^{-1}, employing a Netzsch STA 409 PC Luxx instrument. The elemental analyses were performed using a Thermo FlashEA 1112 Series CHNS-O elemental analyzer with an accepted tolerance of ±2% on carbon (C), hydrogen (H), nitrogen (N) and sulfur (S). X-ray fluorescence (XRF) qualitative analyses were performed under ambient conditions on powdered samples of thermally activated **Zr_BTDZ** and [DCF@**Zr_BTDZ**] using a PANalytical MINIPAL 2 instrument equipped with a sealed X-ray tube with a Cr anode. The generator was set at 30 kV and 3 μA. Scanning electron microscopy (SEM) images of the samples were acquired using a FEI/Philips XL30 ESEM scanning electron microscope. Qualitative elemental analysis was performed with an Ametek element EDX energy dispersive X-ray spectrometer plugged into the above quoted microscope. Powdered samples of **Zr_BTDZ** were deposited on carbon tape and were analysed after metalation with Ni, operating at 1.6×10^{-9} mbar and 20 kV and using a secondary electron detector. The nature and purity of all the batches employed for the functional characterization were assessed through powder X-ray diffraction (PXRD). PXRD qualitative measurements were carried out in the 2.0–50.0° 2θ region with a Panalytical X'PERT PRO diffractometer equipped with a Ni filter in the diffracted beam, a PIXcel© solid state detector and a sealed X-ray tube (Cu Kα, λ = 1.5418 Å). Slits were used on both the incident (Soller slits aperture: 0.25°; divergence slit aperture: 0.5°) and the diffracted (anti-scatter slit aperture: 7.5 mm) beam. The generator was operated at 40 kV and 40 mA. UV-vis absorption diffuse reflectance spectra of H_2BTDZ and **Zr_BTDZ** in the solid state were recorded from 250 to 600 nm with a Jasco V-770 spectrophotometer equipped with a 60 mm integrating sphere and a PbS detector (ISN-923), using an interval wavelength of 1 nm. Fluorescence spectra of H_2BTDZ and **Zr_BTDZ** in the solid state were recorded with a JascoFP-8300 spectrofluorometer equipped with a 150 W Xenon arc lamp. The samples were irradiated at the wavelength corresponding to their maximum absorbance, as revealed by the absorption spectrum. Quantum yield analysis was conducted using an

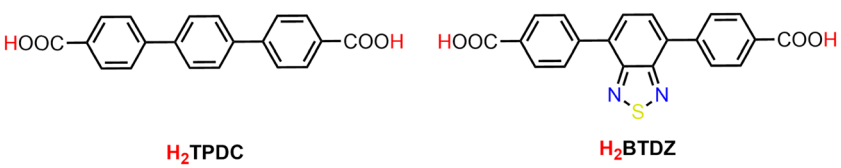

H_2TPDC H_2BTDZ

Scheme 1 The ditopic linkers used in this study for the construction of the UiO-68-type Zr^{IV} MIXMOF **Zr_BTDZ**: (*p*-terphenyl)-4,4″-dicarboxylic acid (H_2TPDC) and 4,4′-(benzothiadiazole-4,7-diyl)dibenzoic acid (H_2BTDZ).

ILF-835 integrating sphere (∅ = 100 mm) connected to the instrument. The optical band gaps of H_2BTDZ and **Zr_BTDZ** in the solid state, 2.58 and 2.65 eV, respectively, were determined from the onset of their absorption spectra.

2.2. Synthesis of Zr_BTDZ

Following the method reported by Lin *et al.* for the preparation of microcrystalline UiO-68,[11] zirconium chloride [$ZrCl_4$, FW = 233.02 g mol^{-1}, 0.070 g, 0.3 mmol] and trifluoroacetic acid (HTFA, 1 mL) were mixed together and diluted with *N,N*-dimethylformamide (DMF, 20 mL). The resulting suspension was sonicated in an ultrasonic bath at ambient temperature for 15 minutes, yielding a clear colorless solution. After that time, H_2TPDC (FW = 318.32 g mol^{-1}, 0.080 g, 0.25 mmol) and H_2BTDZ (FW = 376.38 g mol^{-1}, 0.020 g, 0.05 mmol) were added to the solution; the mixture was further diluted with fresh DMF (30 mL), sonicated for an additional 15 minutes and finally transferred into a Teflon-lined stainless-steel autoclave (inner Teflon beaker volume *ca.* 100 mL). The autoclave was sealed and heated at 393 K for 3 days under autogenous pressure. After slow overnight cooling, a microcrystalline lemon-yellow powder of **Zr_BTDZ·DMF** formed at the bottom of the beaker. It was collected, washed with ethanol (4 × 10 mL) and petroleum ether (4 × 10 mL) and finally dried under a nitrogen stream at room temperature. Yield: 0.115 g [93%, based on the formula $Zr_6O_4(OH)_7(H_2O)_3(TPDC)_3(BTDZ)_{1.5}\cdot 2.5(DMF)$ (*vide infra*)]. Elemental analysis calcd (%) for **Zr_BTDZ·DMF**, $C_{97.5}H_{81.5}N_{5.5}O_{34.5}S_{1.5}Zr_6$ (MW = 2477.76 g mol^{-1}): C 47.26, H 3.32, N 3.11, S 1.94. Elemental analysis found (%): C, 46.83; H, 3.13; N, 3.08; S, 1.79. IR bands (KBr pellet, cm^{-1}, Fig. S1, ESI†): 1680 (s, $[\nu(COO)]_{asym}$), 1606 (s, $[\nu(COO)]_{asym}$), and 1561 (sh, $[\nu(COO)]_{asym}$).

2.3. Powder X-ray diffraction crystal structure characterization

To characterize the crystal structure of **Zr_BTDZ**, powder X-ray diffraction (PXRD) data were acquired in-house under ambient conditions using a Bruker AXS D8 Advance vertical-scan θ:θ diffractometer, equipped with a sealed X-ray tube (Cu K_α, λ = 1.5418 Å), a Bruker Lynxeye linear position-sensitive detector, a filter of nickel in the diffracted beam, and the following optical components: primary- and secondary-beam Soller slits (aperture: 2.5°), fixed divergence slit (aperture: 0.5°), and anti-scatter slit (aperture: 8 mm). The generator was set at 40 kV and 40 mA. After *ex situ* thermal activation [performed at T = 403 K and under high vacuum (10^{-6} Torr) for 24 h], a powdered sample of **Zr_BTDZ** (~50 mg) was deposited into the cavity of a silicon free-background sample-holder 0.2 mm deep (Assing Srl, Monterotondo, Italy). The purity and crystallinity of the sample were checked by carrying out a preliminary PXRD data acquisition in the 2θ range 3.0–35.0°, with steps of 0.02° and a time per step of 1 s. All data treatments described in the following were carried out using the software TOPAS-R v.3.[12] A whole powder pattern refinement with the Le Bail method[13] was performed employing the space group and unit cell parameters of UiO-68[14] as a start. The background was modelled using a Chebyshev polynomial function. The instrumental contribution to the peak profile was described using the fundamental parameters approach.[15] The sample contribution to the peak profile was modelled using a convolution of Lorentzian and Gaussian functions, while the peak anisotropic broadening was described using spherical harmonics. This preliminary data treatment concomitantly confirmed the sample purity and the adequacy of the adopted crystallographic information to successfully describe the PXRD pattern of **Zr_BTDZ**. In addition, as the presence of two different ligands did not imply a symmetry decrease with respect to the parent MOF, a uniform distribution of the two linkers and the absence of homo-linker domains could be supposed. To further characterize the crystal structure, another PXRD pattern was acquired on the same thermally activated sample of **Zr_BTDZ**, working under ambient conditions and taking advantage of the instrumental configuration and sample holder described above. The data were acquired in the 2θ range 3.0–105.0°, with steps of 0.02° and a time per step of 10 s. During all the steps of structure assessment and refinement, the background and instrumental and sample contribution to the peak profile were modelled as detailed above. An isotropic thermal factor, B_{iso}(Zr), was assigned to the Zr^{IV} ions, while the isotropic thermal factor of all the remaining atoms was calculated as $B_{iso} = B_{iso}(Zr) + 2$ Å^2. The crystallographically independent portion of the two linkers was described as rigid body using the *z*-matrix formalism, adopting idealized bond distances and angles.[16] The crystallographically independent zirconium and oxygen atoms forming the inorganic secondary building unit (SBU) were initially assigned the fractional coordinates they possess in the crystal structure of UiO-68.[14] For simplicity, the μ^3-OH^- ions were described exclusively with oxygen atoms. As the two spacers possess the same ter-phenyl dicarboxylate skeleton, a unique planar rigid body was built up (Scheme S2, ESI†), weighting the site occupation factors of the vicariant (H *vs.* N–S) atoms according to the linkers' ratio retrieved *via* ^{1}H-NMR spectroscopy on the digested sample (see above). The position (the centre of the inner phenyl ring occupies the [0.25, 0, 0.25] special position, Wyckoff letter d) and initial orientation of the rigid body were set according to the crystal structure of UiO-68. Subsequently, to improve the agreement between the observed and calculated PXRD patterns, (i) a dummy oxygen atom (reasonably coming from atmospheric humidity adsorption after thermal activation and sample handling in air) modelling smeared electron density within the octahedral and tetrahedral cavities was located employing the simulated annealing approach;[17] (ii) maintaining for the vicariant atoms the ratio disclosed by ^{1}H NMR spectroscopy, the presence of missing-linker defects was verified and resulted in *ca.* 20% of missing ligands. The missing electric charge was supplied binding to the independent zirconium atom an additional oxygen atom (mimicking both a water molecule and a hydroxy group, to grant electroneutrality) vicariant with the oxygen atom of the carboxylate groups. Finally, the structure refinement was carried out with the Rietveld method.[18] At this stage, (i) unit cell parameters, coefficients of the polynomial function describing the background, coefficients of the functions describing the sample contribution to the peak shape and

width, B_{iso}(Zr) were refined without restraints; (ii) the ligands central and peripheral rings were allowed to rotate around the main axis of the linker(s), to verify the presence of rotational disorder; a rotation of the central and peripheral rings by 46.5(4)° and 7(1)°, respectively, granted a slight decrease of the R_p and R_{wp} of the figures of merit; (iii) when not special, hence not fixed, the fractional coordinates of the SBU zirconium and oxygen atoms were refined without imposing restrains; (iv) the rigid body bond distances (except for the C–H ones) were refined in restrained, chemically sensible ranges.[19] The graphical representation of the final stage of the structure refinement is available as Fig. S2 (ESI†). Main crystallochemical information and structure refinement relevant figures of merit are reported below.

Crystallochemical information for **Zr_BTDZ**, $Zr_6O_4(OH)_{6.4}(H_2O)_{2.4}(TPDC)_{3.2}(BTDZ)_{1.6}\cdot 7(H_2O)$: $C_{96}H_{79.6}N_{3.2}O_{39}S_{1.6}Zr_6$, FW = 2500.8 g mol^{-1}, cubic, $Fm\bar{3}m$, a = 32.883(2) Å, V = 35 553.8(7) Å^3, Z = 4, Z' = 0.021, ρ = 0.47 g cm^{-3}, $F(000)$ = 5022.4, R_{Bragg} = 1.6%, R_p = 2.8% and R_{wp} = 4.0%, for 5076 data and 63 parameters in the 3.5–105.0° (2θ) range. CCDC no. 2423400.

2.4. Temperature-resolved powder X-ray diffraction

The thermal behaviour of **Zr_BTDZ** was followed *in situ* by means of temperature-resolved powder X-ray diffraction (TR-PXRD). After thermal activation [T = 403 K under high vacuum (10^{-6} Torr) for 24 h], a powdered sample of **Zr_BTDZ** (~20 mg) was placed in the cavity of an aluminium sample-holder and was heated in air using a custom-made heater (Officina Elettronica di Tenno, Ponte Arche, Italy) spanning the temperature range 303–763 K with steps of 20 K and acquiring a PXRD pattern at each step under isothermal conditions, in the 2θ range 3.5–19.7° with steps of 0.02° and a time per step of 1 s. A parametric whole powder pattern refinement with the Le Bail approach was subsequently performed on all the data.

2.5. Textural properties assessment through N_2 adsorption

A powdered sample (*ca.* 40 mg) of **Zr_BTDZ** was activated at T = 403 K under high vacuum (10^{-6} Torr) for 24 h before the measurement. The Brunauer–Emmett–Teller (BET) specific surface area, pore size distribution and pore volume (V_{tot}, V_{micro}) were estimated by volumetric adsorption with an ASAP 2020 Micromeritics instrument, using N_2 as the adsorbate at 77 K. For the BET specific surface area calculation, the 0.01–0.1 p/p_0 pressure range of the isotherm was used to fit the data. Within this range, all the Rouquerol consistency criteria[20,21] are satisfied. The material (micro)porosity was determined from the N_2 adsorption isotherm using a NLDFT method (Tarazona approximation) and assuming a cylindrical pore shape (typical of metal oxides).

2.6. DCF and IBR luminescence sensing

Luminescence measurements were performed with a Cary Elipse fluorescence spectrometer (excitation source λ = 380 nm) and a quartz cuvette with a total volume of 3 mL and an optical path of 1 cm. A suspension of **Zr_BTDZ** (5 mg in 25 mL of distilled water, sonicated for 30 minutes) was employed to measure the luminescence of the materials; the acquired spectrum was used as a reference to monitor possible differences due to the presence of either DCF or IBR. Successively, 2 mL of the **Zr_BTDZ** suspension were placed in a 3 mL cuvette; known amounts of either DCF or IBR were added, the cuvette was gently shaken and the spectra were recorded. Variation(s) in the intensity of the spectra and/or changes in the value of λ_{max} were recorded. The binding constant (K_b) of DCF and IBR with **Zr_BTDZ** was determined from the emission intensity data following the modified Benesi–Hildebrand equation:

$$\frac{1}{\Delta I} = \frac{1}{\Delta I_{max}} + \frac{1}{[C] \times K_b} \times \frac{1}{\Delta I_{max}}. \quad (1)$$

Here, $\Delta I = I_x - I_0$ and $\Delta I_{max} = I_{max} - I_0$, where I_0, I_x, and I_{max} are the emission intensities of **Zr_BTDZ** considered in the absence of DCF (or IBR), at an intermediate DCF (or IBR) concentration, I_{max} is the intensity of complete saturation and $[C]$ is the pollutant concentration, respectively. The value of K_b has been determined from the slope of the ΔI *vs.* $[C]$ curve. The limit of detection (LOD) for DCF and IBR was evaluated from a linear fitting of the intensity emission *vs.* $[C]$ using the equation LOD = $3\sigma/\rho$, where σ is the standard deviation for repeated fluorescence measurements of blank solution and ρ is the slope of the regression line.[22]

2.7. DCF and IBR adsorption and desorption tests

Adsorption tests were performed by suspending 4 mg of **Zr_BTDZ** in 6 mL of the pharmaceutical; different concentrations were tested, between 5 and 200 mg L^{-1}. The suspensions were left stirring at room temperature for 5 hours; at this point, they were centrifugated and the supernatant was analysed, to determine the concentration of either DCF or IBR. The molecules were detected through UV spectroscopy, as both DCF and IBR absorb in the $220 < \lambda < 380$ nm interval. Data were fitted using the Langmuir adsorption model, according to the equation:

$$\frac{C_e}{q_e} = \frac{1}{X_m \times K} + \frac{C_e}{X_{me}} \quad (2)$$

In the equation, C_e represents the solution concentration of the pollutant at the equilibrium (mg L^{-1}), q_e is the quantity of pollutant adsorbed by a unit of material at the equilibrium (mg g^{-1}) and X_m is the maximum adsorption capacity of the material for a certain pollutant (mg g^{-1}). Tests were also performed with both pollutants at one time in a binary mixture, to assess the preferential adsorption and the removal efficiency of **Zr_BTDZ** under these conditions. To this aim, 4 mg of MOF were placed in 6 mL of a solution containing both analytes; the concentration range used was between (2.5 + 2.5) and (100 + 100) mg L^{-1} for each molecule (*i.e.* a total concentration between 5 and 200 mg L^{-1}). To establish whether the pharmaceuticals were reversibly adsorbed, 4 mg of **Zr_BTDZ** were placed in a solution (6 mL) of either DCF or IBR at 200 mg L^{-1} concentration and left stirring at room temperature for 5 hours. Then the powder was separated from the solution by centrifugation and dried at about 40 °C overnight; successively, it was suspended in 6 mL of distilled water and left stirring for 5 hours. After this time, the powder was separated and the amount of

either DCF or IBR in solution was measured through UV spectroscopy. Luminescence spectra were also acquired for these samples, to establish the possible reversibility of the emission. To test the reusability of the powder, successive adsorption experiments were performed using the same batch. The experimental protocol is the same described above for the desorption test, and it was repeated twice. In addition to the adsorption efficiency, the emission spectra were also acquired to assess the reproducible performance of **Zr_BTDZ** as a luminescence sensor.

2.8. Computational details

All periodic DFT calculations were performed using the CP2K code by employing mixed Gaussian-type plane-wave (GPW) basis sets.[23] Core electrons were represented with norm-conserving Goedecker–Teter–Hutter pseudopotentials,[24–26] and the valence electron wavefunction was expanded in a double-zeta basis set with polarization functions along with an auxiliary plane wave basis set with an energy cutoff of 600 Ry.[27] The generalized gradient approximation exchange–correlation functional of Perdew, Burke and Enzerhof (PBE) was used.[28] Test calculations showed that the total energy change of the reactive system was negligible (<0.01 eV) when the maximum force convergence criterion of 0.00045 hartree bohr^{-1} was used. Each reaction state configuration was optimized with the Broyden–Fletcher–Goldfarb–Shanno (BGFS) algorithm with an SCF convergence criterion of 1.0×10^{-6} a.u. To compensate the long-range van der Waals dispersion interaction between the adducts and the MOF, the DFT-D3 scheme with an empirical damped potential term was added to the energies obtained from exchange–correlation functional in all calculations.[29] The adduct formation energy (E_{ad}) can be evaluated through the following equation:

$$E_{ad} = E_{host+guest} - (E_{host} + E_{guest}) \quad (3)$$

where $E_{host+guest}$ is the total energy of the guest molecule interacting with **Zr_BTDZ**, E_{host} is the total energy of the optimized empty **Zr_BTDZ** and E_{guest} is the energy of the DCF/IBR molecule *in vacuo*. The initial **Zr_BTDZ** guess structure was taken from the PXRD Rietveld refinement, with the lattice constants of $a \times b \times c = 32.8823 \times 32.8823 \times 32.8823$ Å. The framework structure omits unnecessary atoms but it is sufficiently large to describe the main MOF structural properties (such as its octahedral and tetrahedral cavities, Fig. 1c and d).

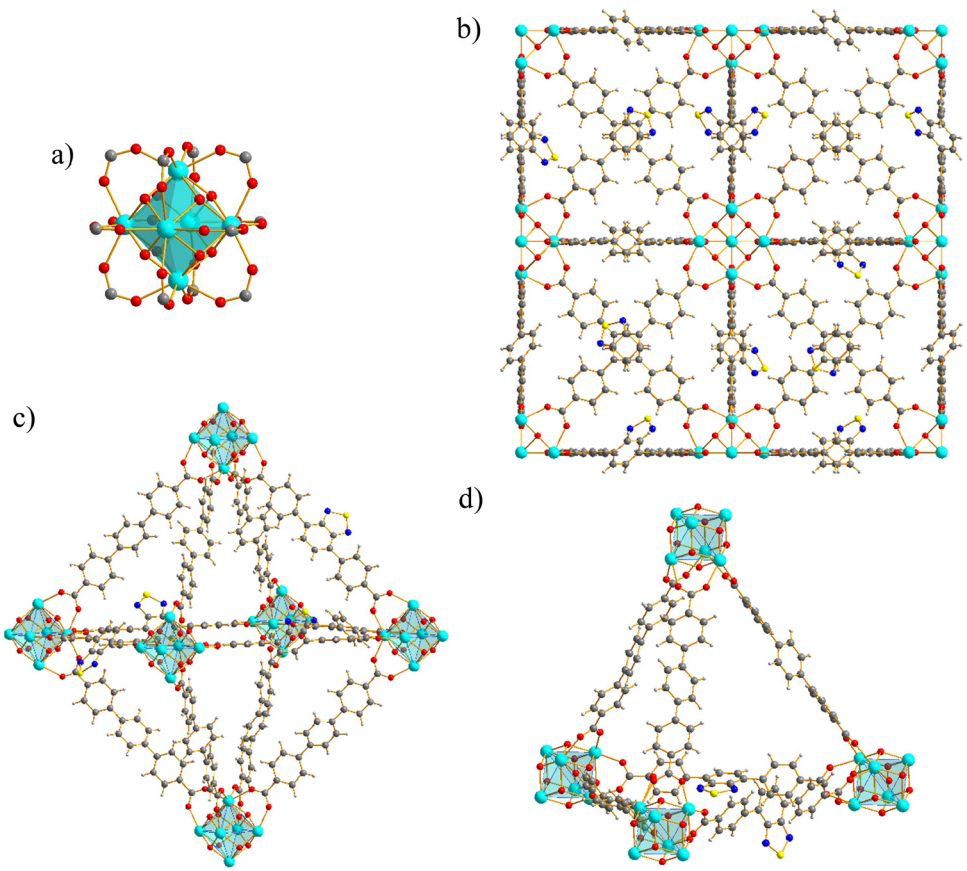

Fig. 1 Representation of the crystal structure of **Zr_BTDZ**: (a) the node. (b) Portion of the 3D open framework visualized along one of the crystallographic axes. (c) The octahedral cavity. (d) The tetrahedral cavity. For the sake of clarity, the pictures were produced employing an ideal structural model without missing-linker defects, rotational disorder of the central ring and oxygen atoms modelling the clathrated water molecules. The ligands were represented according to the BTDZ : TPDC = 1 : 2 ratio retrieved by ^{1}H-NMR. Element colour code: carbon, grey; hydrogen, light grey; nitrogen, blue; oxygen, red; sulphur, yellow; zirconium, cyan.

3. Results and discussion

3.1. Synthesis and characterization of Zr_BTDZ

The mixed-linker MOF **Zr_BTDZ** was prepared through direct synthesis following a typical preparation of UiO-6x MOFs under solvothermal conditions in DMF, using Zr^{IV} chloride as the metal precursor and trifluoroacetic acid as the crystal modulator.[9–11,30–33] Notably, the use of a rather dilute solution is essential to obtain a microcrystalline powder in almost quantitative yields.[11] The PXRD pattern (Fig. S2, ESI†) is very similar to that of UiO-68[11,33] and to those of the relative frameworks UiO-68-Se reported by Wang *et al.* containing the benzoselenadiazole analogue of H_2BTDZ,[34] PCN-57 published by Farha *et al.* (a MIXMOF made with Me_4-H_2TPDC and H_2BTDZ),[35] the homo-linker analogue $[Zr_6O_4(OH)_4(BTDZ)_6]$ by Eddaoudi and co-workers,[36] and a series of isoreticular derivatives of general formula $[Zr_6O_4(OH)_4(BTDZ\text{-}G)_6]$ (G = decorating group on the phenyl rings of $BTDZ^{2-}$) prepared by Li *et al.* in 2021,[37] proving the same **fcu** (cubic) crystal topology typical of all the members of the UiO-6x family. A whole powder pattern refinement proved that **Zr_BTDZ** possesses the same metric of UiO-68 and concomitantly excluded the formation of single-linker segregated phases. IR spectroscopy (Fig. S1, ESI†) confirms the presence of both linkers in the material, considering the typical $[\nu(COO)]_{asym}$ vibrational modes present in the substituted MOF. X-ray fluorescence spectroscopy (Fig. S3, ESI†) preliminarily confirmed the presence of sulphur (and hence that of H_2BTDZ) in the solid; furthermore, it excluded the presence of chlorine in the solid, proof of evidence of the absence of terminal chloride anions on the defective metal coordination sites. Scanning electron microscopy coupled with energy dispersive X-ray spectroscopy (SEM-EDX) (Fig. S4 and S5, ESI†) showed the typical octahedral morphology of UiO-6x MOFs, as well as a uniform distribution of sulfur, indicating that the heterocyclic ligand is homogeneously dispersed in the solid matrix. The nominal linkers stoichiometric ratio, H_2TPDC : H_2BTDZ = 5 : 1, was chosen in order to dilute the luminescent heterocycle into a "fully carbocyclic" MOF with no fluorescence emission in the visible region, thus inhibiting self-quenching phenomena we experienced in the recent past,[10] caused by a too close proximity of the emitters in the crystal structure. The effective relative linkers ratio in the solid was determined through digestion of the MOF in a NaOD/D_2O/DMSO-d_6 solution kept at T = 353 K for 2 h followed by ^{1}H NMR analysis of the resulting solution (Fig. S6, ESI†). A 2 : 1 ratio between the carbocyclic and heterocyclic components was estimated from integration of signals belonging to H_2TPDC and H_2BTDZ. In addition, missing linker defects are present and witnessed by the CHNS elemental analysis (Section 2.2) that shows a lower CHNS content with respect to the hypothetical "defect-free" minimal formula $[Zr_6O_4(OH)_4(TPDC)_4(BTDZ)_2]$. Thermogravimetric analysis (Fig. S7, ESI†) unveiled the high thermal stability of the MIXMOF, with a decomposition temperature T_{dec} = 833 K almost identical to that of UiO-68[33] and higher than that of UiO-68-Se (T_{dec} = 773 K)[34] and of the homo-linker analogue $[Zr_6O_4(OH)_4(BTDZ)_6]$ (T_{dec} = 673 K).[36] A first weight loss of *ca.* 8.0 wt% centered at $T \sim$ 443 K can be ascribed to DMF (theoretical weight loss = 7.4 wt%), in agreement with the presence of its mass peak at m/z = 73 a.m.u. in the mass spectrum of the evolved volatile species (data not shown). A second thermal event centered at $T \sim$ 643 K (weight loss of *ca.* 21.0 wt%) can be reasonably ascribed to the thiadiazole linker decomposition (theoretical weight loss = 22.7 wt%. From an independent measurement, it was found that H_2BTDZ starts decomposing at T = 633 K). After the degradation of the heterocyclic linker, the MOF decomposes leaving a residue corresponding to the tetragonal polymorph of ZrO_2 (experimental residual weight = 29.6 wt%; theoretical residual weight = 29.8 wt%), as also confirmed by a whole powder pattern refinement of the PXRD profile of the solid recovered at the end of the thermal analysis (Fig. S8, ESI†). Differential scanning calorimetry (Fig. S9, ESI†) revealed a single peak centred at 834 K associated to decomposition. The temperature-resolved powder X-ray diffraction experiment performed in air in the range 303–763 K showed that **Zr_BTDZ** maintains its pristine degree of crystallinity up to the highest temperature investigated (Fig. S10a, ESI†), implying that the release of clathrated water and heterocyclic linker witnessed by TGA-MS does not cause a collapse of the framework. A parametric whole powder pattern refinement carried out on the whole dataset with the Le Bail method showed that the material undergoes a unit cell volume contraction as the temperature increases (Fig. S10b, ESI†), in line with the mass loss just quoted. Overall, the percentage relative variations of the cell edge and volume amounts to −0.6% and −1.7% respectively, leading to a volumetric thermal expansion coefficient α_V of -3.7×10^{-5} K^{-1}. Overall, the final minimal formula $[Zr_6O_4(OH)_7(H_2O)_3(TPDC)_3(BTDZ)_{1.5}]$ proposed for the (solvent-free) MIXMOF is derived from the combined ^{1}H NMR, elemental analysis and TGA-MS information.

3.2. Structural features of Zr_BTDZ

As proved by a preliminary whole powder pattern refinement followed by successful structure solution and refinement, **Zr_BTDZ** shares the same cubic space group ($Fm\bar{3}m$) of UiO-68,[14] as well as a unit cell length [a = 32.8823(2) Å] comparable to that of UiO-68 [a = 32.632(8) Å at 100 K], and other UiO-68-type MOFs found in the Cambridge Structural Database [CSD version 2024.1, Cambridge Crystallographic Data Centre, Cambridge, United Kingdom] whose structures were solved under ambient conditions [a = 32.397(1)–33.262 Å]. This occurrence suggests that the two linkers characterizing **Zr_BTDZ** are homogeneously distributed within the crystal structure, without forming homo-linker domains. The crystal structure of **Zr_BTDZ**, here briefly described for the sake of completeness, is characterized by octahedral $[Zr_6(O)_4(OH)_4]^{12+}$ nodes (Fig. 1a) twelve-connected to adjacent ones by six ditopic $TPDC^{2-}$ or $BTDZ^{2-}$ linkers, generating a 3D open framework (Fig. 1b) with **fcu** topology. The framework features octahedral and tetrahedral cavities (Fig. 1c and d) with an approximate diameter of ∼16.1 and ∼8.0 Å, respectively. The central ring of the linker is rotated by about 45° with respect to the main axis of the molecule and

affected by rotational disorder, as already found for other UiO-68-type MOFs.[14] Neglecting the clathrated water molecules (see the Experimental section), the empty volume is about 67% of the unit cell volume, which is lower than the value of about 80% found by Manna *et al.*[11] for UiO-68, as expected based on the lower steric hindrance of $TPDC^{2-}$ with respect to $BTDZ^{2-}$.

3.3. Textural property assessment

The porosity of **Zr_BTDZ** was analysed through N_2 volumetric adsorption at 77 K on a pre-activated powdered sample (Fig. 2). The isotherm shape is of Type I, typical of microporous materials. The BET specific surface area equals 3770 $m^2\ g^{-1}$; it is slightly lower than that of UiO-68 (4170 $m^2\ g^{-1}$)[33] but higher than that of the homo-linker analogue $[Zr_6O_4(OH)_4(BTDZ)_6]$ (2380 $m^2\ g^{-1}$),[36] as expected when the $TPDC^{2-}$ ligand is partially replaced by the more sterically encumbered $BTDZ^{2-}$. The micropore size distribution evaluated through NLDFT methods has disclosed the presence of micropores of *ca.* 18, 22 and 25 Å size (inset in Fig. 2).

3.4. Luminescence properties of Zr_BTDZ and DCF/IBR sensing/adsorption/desorption tests

With the luminescence sensing applicative context in mind, the solid-state UV-vis absorption and fluorescence emission properties of the H_2BTDZ linker and the corresponding MIXMOF **Zr_BTDZ** were preliminary assessed. As already reported in many literature works,[35–37] H_2BTDZ is luminescent, absorbing in the 300–450 nm UV range (Fig. S11, ESI†) and emitting in the light green visible region at $(\lambda_{max})_{em}$ = 525 nm (Fig. 3). Upon coordination to zirconium, the emission maximum of the linker undergoes a slight blue shift: indeed, when irradiated with a suitable wavelength (328 nm, corresponding to the maximum of its absorption spectrum, Fig. S11, ESI†), **Zr_BTDZ** exhibits a strong emission peak in the light green visible region at $(\lambda_{max})_{em}$ = 516 nm (Fig. 3). The electronic transition is ligand-centred and is of π → π* or n → π* nature, as already observed

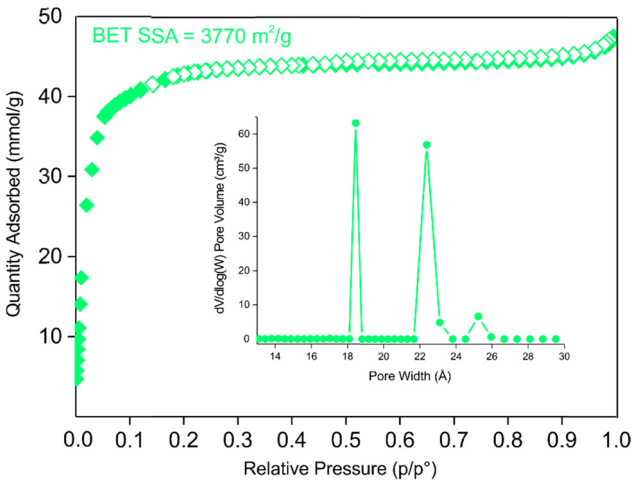

Fig. 2 N_2 isotherm measured at T = 77 K on thermally activated **Zr_BTDZ**. Empty symbols denote the desorption branch. Inset: Micropore size distribution (NLDFT method – Tarazona approximation, cylindrical pore shape).

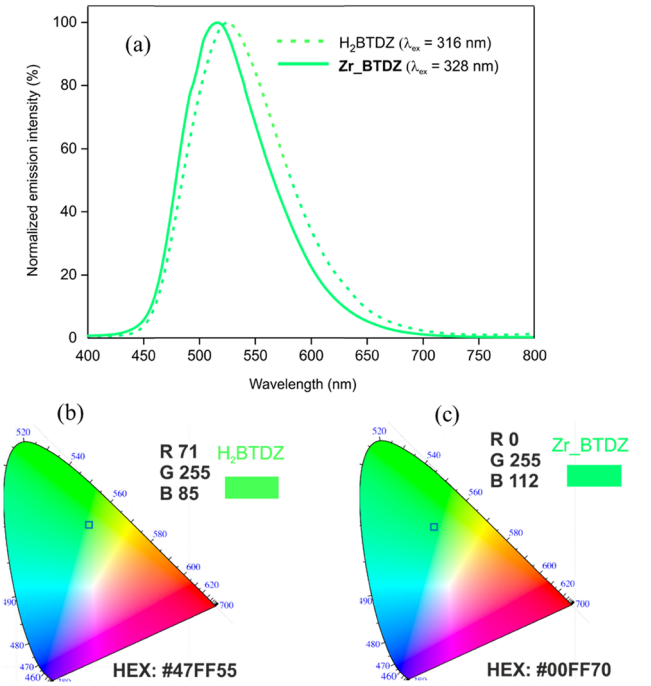

Fig. 3 (a) Normalized emission spectra of H_2BTDZ and **Zr_BTDZ** at comparison. (b) and (c) CIE diagrams of H_2BTDZ and **Zr_BTDZ** derived from the emission spectra, with hexadecimal (HEX) and RGB coordinates of the corresponding emission colour.

for other Zr^{IV} MOFs where the metal ion with its empty d-shell is not involved into any metal-to-ligand or ligand-to-metal charge transfer.[38] The absolute emission intensity of **Zr_BTDZ** is higher than that of free H_2BTDZ: the insertion of the emissive linker within a rigid three-dimensional architecture limits the occurrence of self-quenching effects.[38,39] In line with this statement, the solid-state luminescence quantum yield increases significantly when passing from pure H_2BTDZ (3%) to **Zr_BTDZ** (45%).

The detection of DCF and IBR in water solution was performed through fluorescence sensing. Although it is known from the literature that the structural stability of all the members of the UiO-6x (MIX)MOF family in strongly acidic or basic aqueous suspensions is limited,[10,40–42] the luminescence sensing and adsorption experiments are carried out under almost neutral pH conditions regulated by the pK_b values of DCF (9.8) or IBR (8.7) as sodium salts (pH = 7.1 and 7.6 for DCF and IBR respectively, for a solution where [pollutant] = 1×10^{-4} M), where **Zr_BTDZ** is stable. **Zr_BTDZ** exhibits excellent luminescence stability (the signal did not change significantly even after a prolonged MOF soaking in water for several weeks) and high emission intensity. Upon pollutant addition, the systems reach the equilibrium almost immediately; indeed, the luminescence signal measured just after the addition is the same as those acquired successively in a time lapse of 30 minutes. For both analytes, the variation of **Zr_BTDZ** emission intensity changes according to their concentration. No $(\lambda_{max})_{em}$ (observed at 510 nm) shift occurs upon interaction with the pollutants. However, under irradiation at λ_{ex} = 380 nm **Zr_BTDZ** fluorescence intensity decreased after the addition of

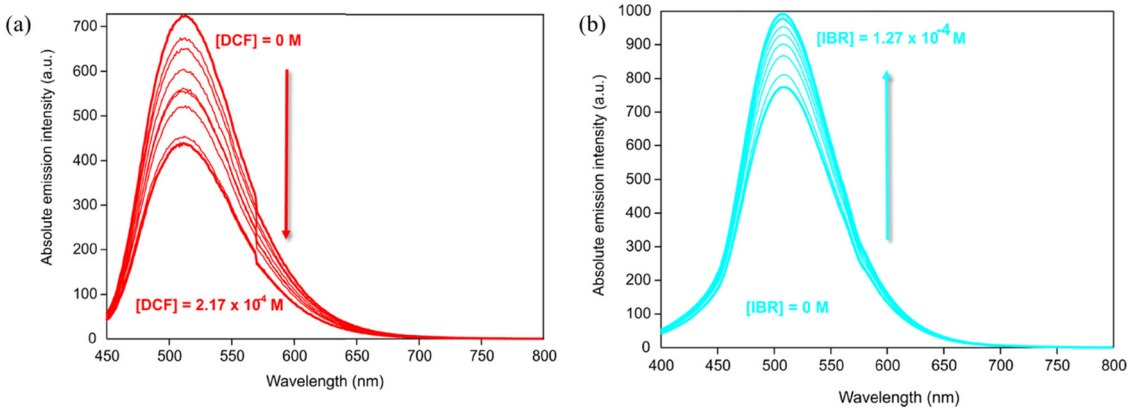

Fig. 4 Emission spectra of **Zr_BTDZ** (λ_{ex} = 380 nm) as a function of DCF (a) and IBR (b) concentration in aqueous solution.

DCF (Fig. 4a), while it increased after the addition of IBR (Fig. 4b). The binding constant values (K_b) and the limit of detection (LOD) of DCF and IBR were determined from the emission intensity data. K_b was evaluated following the modified Benesi–Hildebrand equation, and it was found to be 1.26 × 10^4 M^{-1} and 1.50 × 10^4 M^{-1} for DCF and IBR, respectively (Fig. S12, ESI†). The LOD value for DCF and IBR was estimated to be 4.1 × 10^{-6} M and 1.6 × 10^{-6} M, respectively (Fig. S13, ESI†). These values are better than those measured for TTz@PCN-700 (LOD_{DCF} = 9.0 × 10^{-5} M),[9] $TzPhTz^{Me}$@PCN-700 (LOD_{DCF} = 8.4 × 10^{-6} M)[9] or UiO-67-TzTz (LOD_{DCF} = LOD_{IBR} = 1 × 10^{-4} M).[10] They are one order of magnitude higher than those found in a molecularly imprinted polymer with nanoporous zirconium pyridine-2,6-dicarboxylate Zr-MOF/MIP (LOD_{DCF} = 1 × 10^{-7} M).[43] Their detection capacity is also lower than that found for the composite material UiO-66-NH_2-modified cotton fiber CF@UiO-66-NH_2 reported by Bao and co-workers in 2021 (LOD_{DCF} = 3.8 × 10^{-10} M; LOD_{IBR} = 1.7 × 10^{-8} M).[44] Fluorescence quenching observed with DCF is possibly due to partial electron transfer from the MOF highest occupied crystal orbital (HOCO, Fig. S14, ESI†) to the lowest unoccupied molecular orbital (LUMO, Fig. S15, ESI†) of DCF as a generally well-consolidated quenching mechanism.[38] The guest can act as an energy or electron acceptor, absorbing energy from the excited state of the MOF and dissipating it non-radiatively, thereby reducing the MOF emission. This happens if the guest has suitable electronic levels, such as a low LUMO or an accessible triplet state (energy transfer or photoinduced electron transfer – PET). The fluorescence enhancement observed with IBR (Fig. S16, ESI†) may be caused by the so-called rigidification-induced enhancement, taking place when the guest reduces the internal vibrations or rotations of the luminescent unit (H_2BTDZ in our case), limiting non-radiative decay paths.[36]

Fig. 5a shows **Zr_BTDZ** adsorption isotherms for both pollutants. It can be seen that this MOF shows a better performance with IBR than with DCF, as it reaches saturation for higher IBR concentrations. The data were fitted with the Langmuir model, according to eqn (2) (Fig. S17a, ESI†); it can be seen that for both pharmaceuticals the fitting is very good (R^2 = 0.996 and 0.954 for DCF and IBR, respectively). From the linear fitting, it is possible to infer the maximum adsorption capacity (X_m) values: 100 and 161.3 mg g^{-1} for DCF and IBR, respectively. These values are in line with those reported for other Zr^{IV} (MIX)MOFs of the literature (Table S1, ESI†). The higher affinity of **Zr_BTDZ** for IBR is also confirmed by the removal efficiency (Fig. 5b); both pollutants are completely removed from the solution for concentrations up to 20 mg L^{-1}. The efficiency is higher for IBR even at higher concentrations: a value over 50% was recorded for a concentration as high as 200 mg L^{-1}. In a solution where both pollutants are present simultaneously the removal efficiency decreases. Fig. 5c shows the adsorption isotherms of IBR and DCF; saturation is reached for a lower concentration of the single analyte. This can be explained considering that the adsorption is simultaneous and some of the active sites are already occupied, leading to a reduced adsorption capacity. The fitting with the Langmuir model is not as good as in the case of a single component solution, but still very good correlation values were obtained (R^2 = 0.93 and 0.97 for DCF and IBR, respectively, Fig. S17b, ESI†). The calculated maximum adsorption capacities (X_m) are 41.2 and 64.1 mg g^{-1} for DCF and IBR, respectively. Both values are about 40% of those registered in the single component experiments. These results again confirm higher affinity for IBR in comparison with DCF. However, in a mixed solution there is no preferential adsorption of one over the other. A removal efficiency of 100% was measured for low concentrations (2.5 and 10 mg L^{-1} for each pollutant, *i.e.* 5 and 20 mg L^{-1} in total). For higher concentrations, a better efficiency was observed for IBR (Fig. 5d).

Desorption experiments were performed to assess the process reversibility; results showed an almost complete desorption for DCF (about 75%) and an even higher desorption (about 95%) for IBR. This indicates that the interactions between **Zr_BTDZ** and the pollutants are relatively weak (see Section 3.5). Fig. 6 shows as an example the luminescence spectra acquired for **Zr_BTDZ** after IBR desorption; it can be clearly seen that the luminesce is completely reversible. For DCF desorption a similar behaviour was observed (data not shown).

To test the MOF reusability, repeated adsorption experiments were performed with IBR using the same batch twice. It was found that there is a small decrease in the removal efficiency when passing from the first cycle (100%) to the

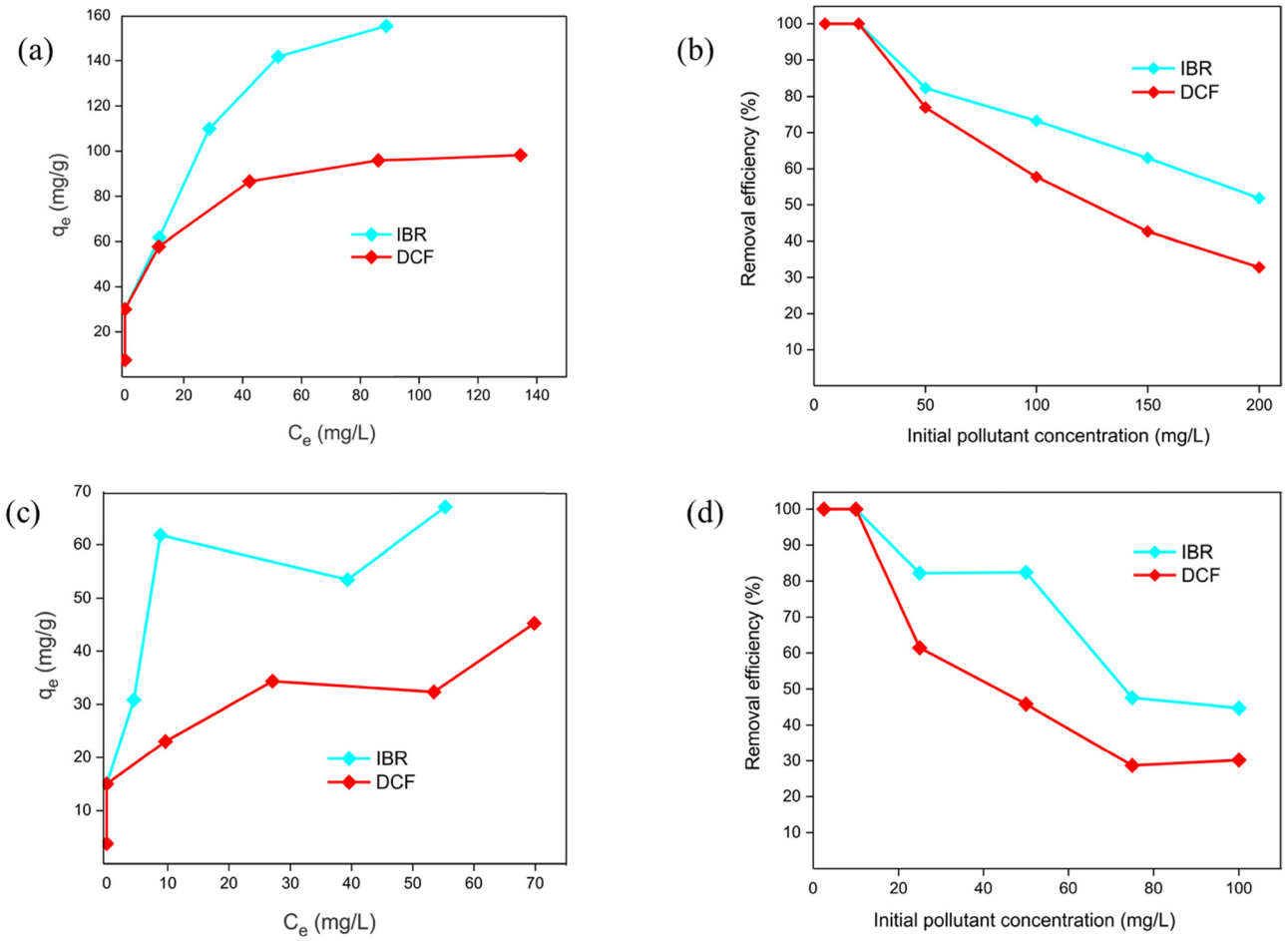

Fig. 5 (a) Adsorption isotherms of **Zr_BTDZ** in pure IBR and DCF solutions. (b) Removal efficiency of **Zr_BTDZ** in pure IBR and DCF solutions. (c) Adsorption isotherms of **Zr_BTDZ** for IBR and DCF binary mixtures. (d) Removal efficiency of **Zr_BTDZ** in IBR and DCF binary mixtures. In (c) and (d) the *X*-axis shows the single analyte concentration.

second cycle (98.4%). This could also be due to the unavoidable sample loss during the workup procedures in the successive cycles of adsorption and washing. Fig. S18 (ESI†) shows the related emission spectra; a small emission intensity difference between the first and second cycle was recorded, in line with the adsorption/desorption experiments. A similar behaviour was observed with DCF (data not shown).

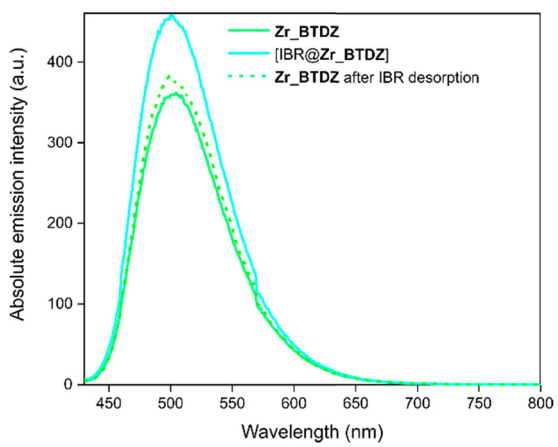

Fig. 6 Luminescence spectra acquired for **Zr_BTDZ** after IBR adsorption and desorption.

3.5. DFT calculation of the electronic structure of Zr_BTDZ and its DCF/IBR adducts

To gain further insight into the possible sensing mechanism, model structures of the [DCF@**Zr_BTDZ**] and [IBR@**Zr_BTDZ**] systems were generated, locating the pollutants in the MOF octahedral cavity and re-optimizing the ensemble. As shown in Fig. 7, we considered two adsorption sites close to the $[Zr_6(O)_4(OH)_4]^{12+}$ nodes: interaction with one $BTDZ^{2-}$ linker (site-1) or interaction with two $BTDZ^{2-}$ linkers (site-2). At site-1, the interaction energies of IBR and DCF are −213.7 and −187.1 kJ mol^{-1}, respectively. At site-2, the interaction energies of IBR and DCF are −228.2 and −192.5 kJ mol^{-1}, respectively. This confirms that in all cases the MOF affinity for IBR is slightly higher than that for DCF (in line with the experimental values of the related binding constants and higher adsorption efficiency, Section 3.4) and it reveals that site-2 is more energetically favorable than site-1 for the drugs

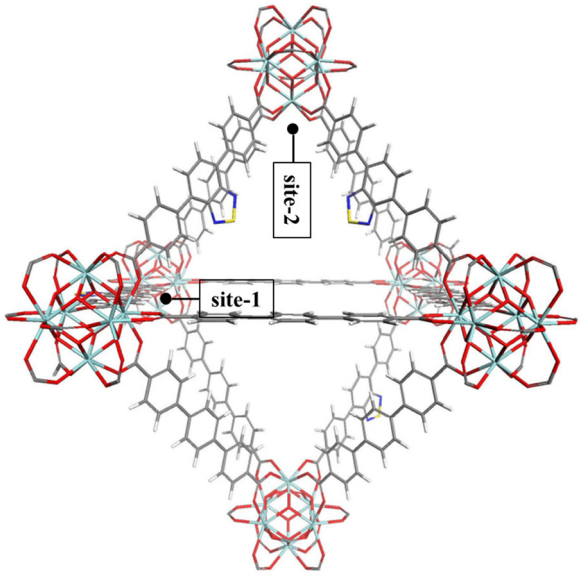

Fig. 7 The two drug adsorption sites in the octahedral cavity of **Zr_BTDZ** were taken into account in the computational study.

adsorption (*i.e.*, the interaction between the drug molecules and two $BTDZ^{2-}$ linkers at one time is stronger than that with only one $BTDZ^{2-}$ linker). The optimized structures are shown in Fig. 8. Although the adsorbed drugs do not form chemical bonds with the MOF, the adsorption site close to the metal nodes and the high number of non-covalent host–guest interactions present in the system generate a strong adsorption capacity for **Zr_BTDZ**. Non-covalent host–guest interactions are present: hydrogen bonding between the μ-OH groups of the inorganic building unit (IBU) and the IBR/DCF carboxylate groups, π–π T-shaped/π–cation interactions between the IBR/DCF aromatic rings/Na^+ ion and the MOF aromatic linkers. Furthermore, the adsorbed DCF molecules show intermolecular hydrogen bonding interactions (N–H···O) that trigger a DCF–DCF *vs.* DCF-MOF competitive adsorption. This is further proof of evidence that the MOF affinity for DCF is lower than that for IBR. The lack of covalent bond is in agreement with the desorption experiments data (Section 3.4), as both pollutants are desorbed from the MOF almost completely. As for the frontier orbitals compositions, in [DCF@**Zr_BTDZ**] (site-2) the HOCO is dominated by the electronic levels of $BTDZ^{2-}$ while the lowest unoccupied crystal orbital (LUCO) is located on the DCF guest (Fig. 9). In addition, the DCF–DCF intramolecular hydrogen bonding interactions are also present in the LUCO, thereby reducing the adsorption interaction with the MOF. For [IBR@**Zr_BTDZ**] (site-2), both HOCO and LUCO are dominated

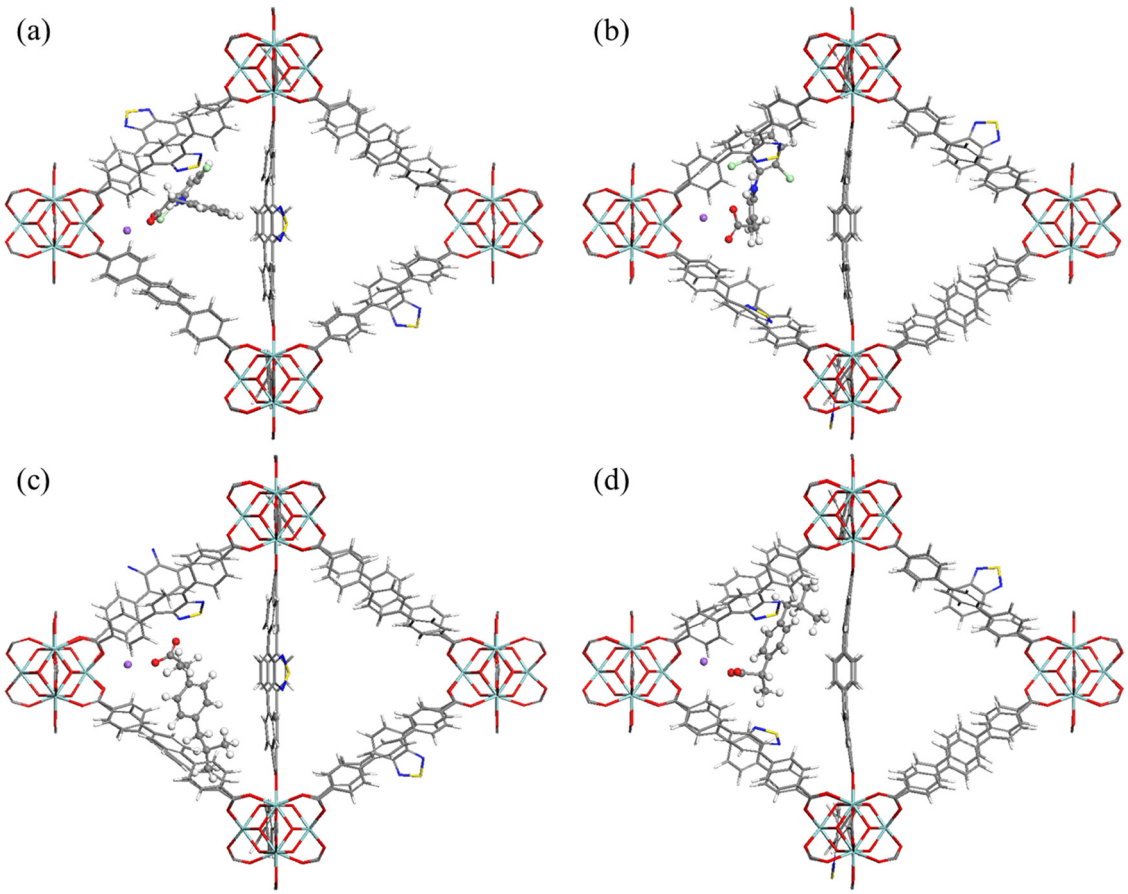

Fig. 8 Optimized structures of (a) [DCF@**Zr_BTDZ**] (site-1); (b) [DCF@**Zr_BTDZ**] (site-2); (c) [IBR@**Zr_BTDZ**] (site-1); (d) [IBR@**Zr_BTDZ**] (site-2). Color scheme: Zr, cyan; O, red; C, grey; H, white; N, blue; S, yellow; Na, purple; Cl, light green.

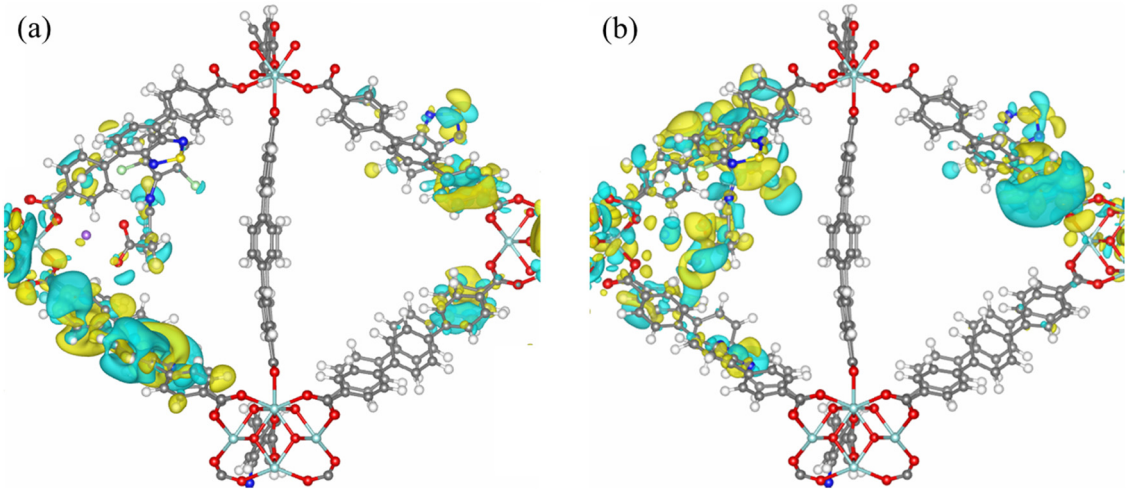

Fig. 9 (a) HOCO and (b) LUCO of [DCF@**Zr_BTDZ**] (site-2).

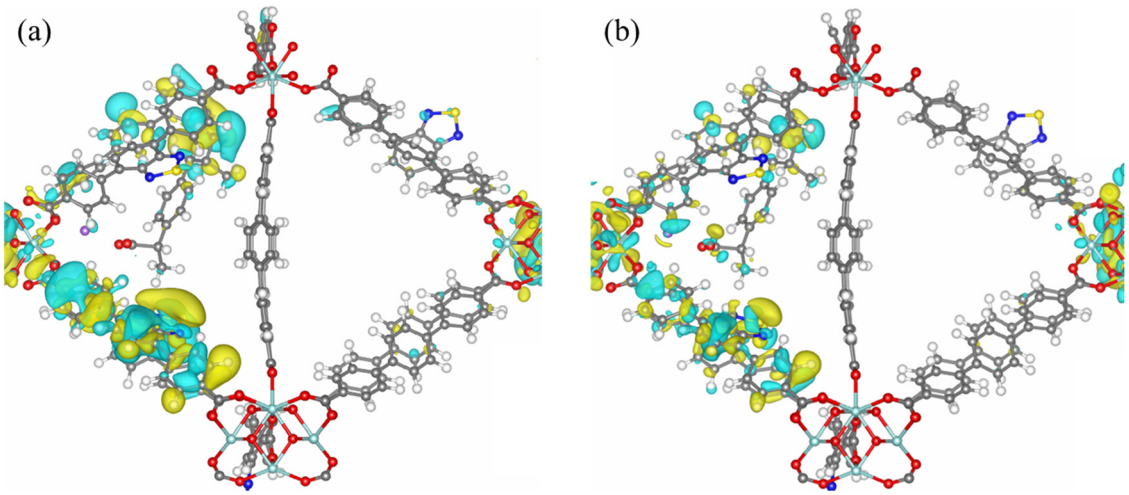

Fig. 10 (a) HOCO and (b) LUCO of [IBR@**Zr_BTDZ**] (site-2).

by the electronic levels of $BTDZ^{2-}$ (Fig. 10). Consequently, the electrons are more localized on the MOF framework indicating that this adsorption state is a physical adsorption with a weak IBR-MOF interaction that facilitates the adsorption–desorption reversibility. Upon adsorption of the guest molecule IBR/DCF, additional energy levels mainly coming from the guest are present and they are located in the HOCO–LUCO band gap of the empty MOF (Fig. S14, ESI†).

4. Conclusions

The new mixed-linker MOF **Zr_BTDZ** containing a benzothiadiazole-based luminescent linker has been prepared and fully characterized in the solid state. Its performance as a luminescent pollutant sensor and adsorbent has been evaluated toward two widespread anti-inflammatory drugs: diclofenac and ibuprofen. Its emission intensity was found to decrease as a function of DCF concentration while it was found to increase proportionally with IBR concentration in water solution. The opposite emission trend is useful to discriminate between the two pollutants, and it may be taken as direct proof of evidence of their presence in wastewater samples. The limit of detection is lower and the adsorption capacity is higher for IBR; both parameters indicate a preferential interaction with this pollutant. The adsorption/sensing process is completely reversible, and the MOF is stable in water suspensions at neutral pH values. Overall, **Zr_BTDZ** represents a good material for this applicative target, and further efforts are ongoing in our laboratories in the direction of the synthesis of better-performing zirconium MOFs for the same application.

Author contributions

G. P., G. B., A. C., and A. M., J. F.: investigation and formal analysis; G. T. and G. G.: validation; D. L.: supervision, methodology, software, and writing – original draft; C. P.: investigation, formal analysis, and writing – original draft; S. G.: supervision, methodology, and writing – original draft; A. R.:

conceptualization, funding acquisition, project administration, supervision, and writing – original draft.

Conflicts of interest

The authors have no conflicts of interest to declare.

Data availability

The data supporting this article have been included as part of the ESI.† Crystallographic data for **Zr_BTDZ** have been deposited at the CCDC with deposition number 2423400.†

Acknowledgements

A. R., G. B., C. P. and S. G. would like to acknowledge the Italian Ministry of University and Research (MUR) and the European Union (Next Generation EU) for funding this research activity through the PRIN 2022 project LUMIMOF (2022A3XNWJ) ''Wastewater treatment and monitoring with luminescent mixed-linker Metal–Organic Frameworks as chemical sensors and adsorbents of contaminants of emerging concern''. A. R. is also grateful to Dr Daniele Franchi and Dr Massimo Calamante (CNR-ICCOM) for precious help with the luminescence quantum yield measurements. C. P. and A. C. would like to thank the Italian Ministry of Research (MUR) for supporting this work through the complementary actions to the PNRR ''Fit4MedRob'' Grant (PNC0000007, CUP B53C22006960001).

References

1 **https://commission.europa.eu/strategy-and-policy/priorities-2019-2024/european-green-deal_en** (last access: June 2025).
2 **https://environment.ec.europa.eu/topics/water/water-framework-directive_en** (last access: June 2025).
3 **https://environment.ec.europa.eu/topics/water/urban-waste-water_en** (last access: June 2025).
4 C. Chen, L. Fei, B. Wang, J. Xu, B. Li, L. Shen and H. Lin, *Small*, 2024, **20**, 2305066.
5 F. Zadehahmadi, N. T. Eden, H. Mahdavi, K. Konstas, J. I. Mardel, M. Shaibani, P. C. Banerjee and M. R. Hill, *Environ. Sci.: Water Res. Technol.*, 2023, **9**, 1305–1330.
6 H. Kaur, N. Devi, S. S. Siwal, W. F. Alsanie, M. K. Thakur and V. K. Thakur, *ACS Omega*, 2023, **8**, 9004–9030.
7 F. Yang, M. Du, K. Yin, Z. Qiu, J. Zhao, C. Liu, G. Zhang, Y. Gao and H. Pang, *Small*, 2022, **18**, 2105715.
8 F. Ahmadijokani, A. Ghaffarkhah, H. Molavi, S. Dutta, Y. Lu, S. Wuttke, M. Kamkar, O. J. Rojas and M. Arjmand, *Adv. Funct. Mater.*, 2024, **34**, 2305527.
9 G. Provinciali, A. L. Capodilupo, A. Mauri, S. Galli, L. Donà, B. Civalleri, G. Tuci, G. Giambastiani, C. Piccirillo and A. Rossin, *ACS ES&T Water*, 2024, **4**, 2339–2351.
10 G. Mercuri, M. Moroni, S. Galli, C. Piccirillo, A. Capodilupo, G. Tuci, G. Giambastiani and A. Rossin, *Inorg. Chem. Front.*, 2022, **9**, 90–102.
11 K. Manna, P. Ji, Z. Lin, F. X. Greene, A. Urban, N. C. Thacker and W. Lin, *Nat. Commun.*, 2016, **7**, 12610.
12 *Topas, V.3.0*, Bruker AXS, Karlsruhe, Germany, 2005.
13 A. Le Bail, *Powder Diffr.*, 2005, **20**, 316–326.
14 A. Schaate, P. Roy, A. Godt, J. Lippke, F. Waltz, M. Wiebcke and P. Behrens, *Chem. – Eur. J.*, 2011, **17**, 6643–6651.
15 R. W. Cheary and A. A. Coelho, *J. Appl. Cryst.*, 1992, **25**, 109–121.
16 The following values were adopted to build the rigid body modelling the independent portion of the ligands: endocyclic bond distances (Å): C–C = 1.40; C–N = 1.36; N–S = 1.66; exocyclic bond distances (Å): C–C = 1.47–1.52; C–O = 1.30; C–H = 0.95; hexatomic rings bond angles (°): 120; pentatomic ring exocyclic bond angles (°): C–C–N = 126; pentatomic ring endocyclic bond angles (°): C–N–S = 106.
17 A. A. Coelho, *J. Appl. Crystallogr.*, 2000, **33**, 899–908.
18 R. A. Young, *The Rietveld Method*, IUCr Monograph N.5, Oxford University Press, Oxford, 1981.
19 The following ranges were adopted to refine the ligands bond distances: endocyclic bond distances (Å): C–C = 1.38–1.42; C–N = 1.32–1.38; N–S = 1.58–1.66; exocyclic bond distances (Å): C–C = 1.47–1.52; C–O = 1.20–1.30.
20 D. A. Gómez-Gualdrón, P. Z. Moghadam, J. T. Hupp, O. K. Farha and R. Q. Snurr, *J. Am. Chem. Soc.*, 2016, **138**, 215–224.
21 J. Rouquerol, P. Llewellyn and F. Rouquerol, in *Studies in Surface Science and Catalysis*, ed. P. L. Llewellyn, F. Rodriquez-Reinoso, J. Rouquerol and N. Seaton, Elsevier, Amsterdam, 2007, vol. 160, p. 49.
22 D. Yu, W. Deng and X. Wei, *Dyes Pigm.*, 2023, **210**, 110968.
23 J. VandeVondele, M. Krack, F. Mohamed, M. Parrinello, T. Chassaing and J. Hutter, *Comput. Phys. Commun.*, 2005, **167**, 103–128.
24 M. Krack and M. Parrinello, *Phys. Chem. Chem. Phys.*, 2000, **2**, 2105–2112.
25 C. Hartwigsen, S. Goedecker and J. Hutter, *Phys. Rev. B: Condens. Matter Mater. Phys.*, 1998, **58**, 3641–3662.
26 S. Goedecker, M. Teter and J. Hutter, *Phys. Rev. B: Condens. Matter Mater. Phys.*, 1996, **54**, 1703–1710.
27 J. VandeVondele and J. Hutter, *J. Chem. Phys.*, 2007, **127**, 114105.
28 J. P. Perdew, K. Burke and M. Ernzerhof, *Phys. Rev. Lett.*, 1996, **77**, 3865–3868.
29 S. Grimme, J. Antony, S. Ehrlich and H. Krieg, *J. Chem. Phys.*, 2010, **132**, 154104.
30 G. Mercuri, M. Moroni, A. Fermi, G. Bergamini, S. Galli, G. Giambastiani and A. Rossin, *Inorg. Chem.*, 2020, **59**, 15832–15841.
31 P. Müller, B. Bucior, G. Tuci, L. Luconi, J. Getzschmann, S. Kaskel, R. Q. Snurr, G. Giambastiani and A. Rossin, *Mol. Syst. Des. Eng.*, 2019, **4**, 1000–1013.
32 S. Yuan, W. Lu, Y.-P. Chen, Q. Zhang, T.-F. Liu, D. Feng, X. Wang, J. Qin and H.-C. Zhou, *J. Am. Chem. Soc.*, 2015, **137**, 3177–3180.
33 J. H. Cavka, S. Jakobsen, U. Olsbye, N. Guillou, C. Lamberti, S. Bordiga and K. P. Lillerud, *J. Am. Chem. Soc.*, 2008, **130**, 13850–13851.

34 W.-Q. Zhang, Q.-Y. Li, Q. Zhang, Y. Lu, H. Lu, W. Wang, X. Zhao and X.-J. Wang, *Inorg. Chem.*, 2016, **55**, 1005–1007.
35 S. Goswami, C. E. Miller, J. L. Logsdon, C. T. Buru, Y.-L. Wu, D. N. Bowman, T. Islamoglu, A. M. Asiri, C. J. Cramer, M. R. Wasielewski, J. T. Hupp and O. K. Farha, *ACS Appl. Mater. Interfaces*, 2017, **9**, 19535–19540.
36 A. Mallick, A. M. El-Zohry, O. Shekhah, J. Yin, J. Jia, H. Aggarwal, A.-H. Emwas, O. F. Mohammed and M. Eddaoudi, *J. Am. Chem. Soc.*, 2019, **141**, 7245–7249.
37 S. Wu, D. Ren, K. Zhou, H.-L. Xia, X.-Y. Liu, X. Wang and J. Li, *J. Am. Chem. Soc.*, 2021, **143**, 10547–10552.
38 G. Mercuri, G. Giambastiani and A. Rossin, *Inorganics*, 2019, **7**, 144.
39 X. Y. Liu, W. P. Lustig and J. Li, *ACS Energy Lett.*, 2020, **5**, 2671–2680.
40 B. Pramanik, R. Sahoo and M. C. Das, *Coord. Chem. Rev.*, 2023, **493**, 215301.
41 D. Bůžek, S. Adamec, K. Lang and J. Demel, *Inorg. Chem. Front.*, 2021, **8**, 720–734.
42 J. B. DeCoste, G. W. Peterson, H. Jasuja, T. G. Glover, Y.-G. Huang and K. S. Walton, *J. Mater. Chem. A*, 2013, **1**, 5642–5650.
43 M. Malekzadeh, A. Mohadesi, M. A. Karimi and M. Ranjbar, *Anal. Bioanal. Electrochem.*, 2020, **12**, 402–414.
44 Y. Gao, S. Wang, N. Zhang, X. Xu and T. Bao, *J. Chromatogr. A*, 2021, **1652**, 462349.